INSTITUT DE FRANCE
Académie des sciences

Comptes Rendus

Physique

Kais Ammar, Benoît Appolaire and Samuel Forest

Splitting of dissolving precipitates during plastic shear: A phase field study

Volume 22, issue S3 (2021), p. 353-370

<https://doi.org/10.5802/crphys.82>

Part of the Special Issue: Plasticity and Solid State Physics

Guest editors: Samuel Forest (Mines ParisTech, Université PSL, CNRS, France) and David Rodney (Université Claude Bernard Lyon 1, France)

Comptes Rendus
Physique
2021, 22, nº S3, p. 353-370
https://doi.org/10.5802/crphys.82

Plasticity and Solid State Physics / *Plasticité et Physique des Solides*

Splitting of dissolving precipitates during plastic shear: A phase field study

Kais Ammar [a], Benoît Appolaire [b, c] and Samuel Forest* [, a]

[a] MINES ParisTech, PSL University, Centre des matériaux (CMAT), CNRS UMR 7633, BP 87 91003 Evry, France.

[b] Université de Lorraine, Institut Jean Lamour, Nancy, France

[c] Labex DAMAS, Université de Lorraine, France.

E-mails: kais.ammar@mines-paristech.fr (K. Ammar), benoit.appolaire@univ-lorraine.fr (B. Appolaire), samuel.forest@mines-paristech.fr (S. Forest)

Abstract. Using a phase field model, we have investigated the role of plasticity on the morphological evolution of a precipitate during its diffusion-controlled dissolution, when submitted to shear loading. It is shown that the plastic strain pattern in the matrix strongly influences the local dissolution rate and consequently the final shape of the precipitate. Finally, it is demonstrated that for sufficiently fast and intense shear loadings, plasticity can induce splitting of the precipitate: this process could explain why small precipitates are observed in shear bands in Ti alloys forged parts.

Keywords. Phase field, Plasticity, Morphology, Shape bifurcation, Dissolution, Titanium alloys.

Available online 8th September 2021

1. Introduction

The influence of elasticity on diffusion controlled phase transformations at the solid state has been extensively investigated. Besides its effect on thermodynamic equilibrium and its consequence on phase diagrams [6], the role of elasticity on morphologies has been largely demonstrated (e.g. [9, 13, 22, 27, 30] to cite a few works among many others). However, it has often been claimed that at high homologous temperatures plasticity is likely to relax completely any elastic contribution, such that the diffusive phase transformations can be investigated without accounting for mechanics. It is only recently, with the development of phase field models coupled with continuum plasticity [2–5, 8, 10, 17–19, 25, 28], that it has become possible to show that the effect of elasticity cannot be discarded even at high temperatures. Indeed, due to the fact that stress relaxation is only partial, plasticity may increase the sizes of the microstructures without changing the nature of the shapes [10]. The impact of plasticity on the patterns formed by assemblies of precipitates can be more spectacular [11, 12]. Moreover, plasticity has been shown to feature

* Corresponding author.

non trivial effects on kinetics, either promoting [2] or impeding [3] interface migration depending on the morphology and loading. Finally, when plasticity displays some viscous character, the evolution is dependent on the ratio of time scales between visco-plasticity and diffusion [24].

Along this line, we address in the present work the possible role of plasticity on shape bifurcation of hard precipitates during mechanical loading at high temperatures, a feature that has never been put into evidence although it can be of interest in hot working of two phase alloys. Indeed, beside the interest for understanding such strong coupling between diffusion controlled phase transformation and plasticity, our work aims at bringing some possible explanation for microstructure evolutions observed commonly during adiabatic shear banding in two-phase Ti alloys. It is indeed not clear whether the small precipitates observed in shear bands results from the deformation process alone or from some partial dissolution due to the local temperature increase. In particular, we will show that the concomitant actions of both plasticity and dissolution are necessary for splitting precipitates into smaller ones. For that purpose, we have used a phase field coupled with an isotropic plasticity model as proposed in [2], that is recalled briefly in the following section. After providing the data and settings of the calculations, we analyze the process of dissolution assisted by shear loading, and on the basis of this analysis, we propose a possible new scenario for explaining the evolution of microstructures in adiabatic shear bands in Ti alloys. Regarding notations, tensors of first, second and fourth rank are respectively denoted by $\underline{\mathbf{u}}, \underset{\sim}{\boldsymbol{\varepsilon}}$ and $\underset{\approx}{\boldsymbol{C}}$.

2. Description of the model

Considering diffusion-controlled phase transformations in alloys, the basic fields describing the microstructure are (i) the phase field $\phi(\underline{\mathbf{r}}, t)$ discriminating the precipitate (α phase) and the matrix (β phase), and (ii) the concentration $c(\underline{\mathbf{r}}, t)$ of an alloying species (here arbitrarily taken as α-stabilizer, although the model can easily be extended to multicomponent alloys). Because mechanics is involved, displacement vector field $\underline{\mathbf{u}}(\underline{\mathbf{r}}, t)$ is the third degree of freedom in the model.

The evolution rates of ϕ and c are governed respectively by the Ginzburg–Landau time-dependent equation and the diffusion equation, relating the rates to their corresponding driving forces as follows:

$$\frac{\partial \phi}{\partial t} = -M \frac{\delta F}{\delta \phi} \tag{1}$$

$$\frac{\partial c}{\partial t} = \nabla \cdot \left(L \nabla \frac{\delta F}{\delta c} \right) \tag{2}$$

where F is the total free energy which is the relevant thermodynamic potential in isothermal conditions. δ denotes functional derivatives, and the mobilities M and L are strictly positive real numbers (isotropy of the corresponding properties are assumed for simplicity). L can be related to the interdiffusion coefficient D as follows $L = D/(\partial^2 f/\partial c^2)$ where f is the free energy density, so as to recover usual diffusion equations in the bulk phases. The stress tensor $\underset{\sim}{\boldsymbol{\sigma}}$, defined as the functional derivative with respect to the strain tensor $\underset{\sim}{\boldsymbol{\varepsilon}}$, fulfills mechanical static equilibrium:

$$\nabla \cdot \underset{\sim}{\boldsymbol{\sigma}} = \nabla \cdot \frac{\delta F}{\delta \underset{\sim}{\boldsymbol{\varepsilon}}} = 0 \tag{3}$$

in the absence of body forces. The free energy functional is decomposed into chemical F_{ch}, elastic F_{el} and plastic F_{pl} contributions.

$$F = F_{\mathrm{ch}}(c, \phi) + F_{\mathrm{el}}(\phi, \underset{\sim}{\boldsymbol{\varepsilon}}) + F_{\mathrm{pl}}\left(\phi, \underset{\sim}{\boldsymbol{\varepsilon}}, \mathcal{V}_{\mathrm{int}}\right) \tag{4}$$

where $\mathcal{V}_{\text{int}}$ is the set of internal variables associated with material hardening. The chemical contribution accounts for the bulk chemical free energy density f_0 and the interface contribution through the gradient squared of ϕ.

$$F_{\text{ch}}(c,\phi) = \int_V dV \left[f_0(c,\phi) + \epsilon |\nabla\phi|^2 \right] \tag{5}$$

where ϵ is a positive real number. The bulk chemical free energy density is approximated by a simple Landau polynomial with respect to ϕ:

$$f_0(c,\phi) = \frac{k}{2}\left(c - A(\phi)\right)^2 + W\phi^2\left(1-\phi\right)^2 \tag{6}$$

where $A(\phi) = c_\beta^e + (c_\alpha^e - c_\beta^e)\,h(\phi)$ and $h(\phi) = \phi^2(3-2\phi)$. c_ψ^e is the equilibrium concentration of phase $\psi \in \alpha,\beta$ provided by the phase diagram at the relevant temperature, and W is the positive height of the double well potential. It is worth noting that the curvature k is the same for both phases, for the sake of simplicity. ϵ and W are related to the interface energy Λ and thickness δ:

$$\epsilon = \frac{3\Lambda\delta}{Z} \quad \text{and} \quad W = 6Z\Lambda/\delta \tag{7}$$

with $Z = \ln[(1-\theta)/\theta]$ assuming that the interface is defined by values of ϕ ranging from θ to $1-\theta$ (in the present work $\theta = 0.05$).

In the framework of linear elasticity, the elastic energy is as usual a quadratic function of the elastic strain tensor $\underset{\sim}{\boldsymbol{\varepsilon}}^{\text{e}}$:

$$F_{\text{el}} = \frac{1}{2}\int_V dV\, \underset{\sim}{\boldsymbol{\varepsilon}}^{\text{e}} : \underset{\approx}{\boldsymbol{C}} : \underset{\sim}{\boldsymbol{\varepsilon}}^{\text{e}} \tag{8}$$

where $\underset{\approx}{\boldsymbol{C}}$ stands for the effective elastic moduli tensor, expressed as a mixture of the elasticity tensors of the individual phases:

$$\underset{\approx}{\boldsymbol{C}} = \underset{\approx}{\boldsymbol{C}}_\beta + \left(\underset{\approx}{\boldsymbol{C}}_\alpha - \underset{\approx}{\boldsymbol{C}}_\beta\right) h(\phi) \tag{9}$$

According to the strain decomposition in the small strain framework, the total strain $\underset{\sim}{\boldsymbol{\varepsilon}}$ is split into three contributions:

$$\underset{\sim}{\boldsymbol{\varepsilon}} = \frac{1}{2}\left(\nabla\underset{\sim}{\boldsymbol{u}} + \nabla\underset{\sim}{\boldsymbol{u}}^T\right) = \underset{\sim}{\boldsymbol{\varepsilon}}^{\text{e}} + \underset{\sim}{\boldsymbol{\varepsilon}}^{\star} + \underset{\sim}{\boldsymbol{\varepsilon}}^{\text{p}} \tag{10}$$

where $\underset{\sim}{\boldsymbol{\varepsilon}}^{\star}$ is the stress-free strain or eigenstrain tensor, accounting for the change in lattice structure from β to α. Based on the application of the Voigt homogenization scheme inside the smooth interface zone as proposed in [2,24], the (visco)-elasto-plastic behaviour of each phase is treated independently, where plastic strain and hardening state of α and β phases at a given time are completely described by a finite number of local internal variables, defined at each point for each phase. As shown in [2,24], according to this scheme the eigenstrain reads:

$$\underset{\sim}{\boldsymbol{\varepsilon}}^{\star} = \underset{\approx}{\boldsymbol{C}}^{-1} : \left[\underset{\approx}{\boldsymbol{C}}_\beta : \underset{\sim}{\boldsymbol{\varepsilon}}_\beta^{\star} + \Delta\underset{\approx}{\boldsymbol{C}}^{\star}\, h(\phi) \right] \tag{11}$$

where $\Delta\underset{\approx}{\boldsymbol{C}}^{\star} = (\underset{\approx}{\boldsymbol{C}}_\alpha : \underset{\sim}{\boldsymbol{\varepsilon}}_\alpha^{\star} - \underset{\approx}{\boldsymbol{C}}_\beta : \underset{\sim}{\boldsymbol{\varepsilon}}_\beta^{\star})$. For the sake of simplicity, it is assumed to be independent of concentration and temperature. Hence, according to the Voigt homogenization scheme, the plastic strain $\underset{\sim}{\boldsymbol{\varepsilon}}^{p}$ reads:

$$\underset{\sim}{\boldsymbol{\varepsilon}}^{p} = \underset{\approx}{\boldsymbol{C}}^{-1} : \left[\underset{\approx}{\boldsymbol{C}}_\beta : \underset{\sim}{\boldsymbol{\varepsilon}}_\beta^{p} + \Delta\underset{\approx}{\boldsymbol{C}}^{p}\, h(\phi) \right] \tag{12}$$

where $\Delta\underset{\approx}{\boldsymbol{C}}^{p} = (\underset{\approx}{\boldsymbol{C}}_\alpha : \underset{\sim}{\boldsymbol{\varepsilon}}_\alpha^{p} - \underset{\approx}{\boldsymbol{C}}_\beta : \underset{\sim}{\boldsymbol{\varepsilon}}_\beta^{p})$.

Still assuming that the elasto-plastic behaviour of each phase is treated independently, an isotropic von Mises rate-independent plasticity without hardening (meaning that $F_{\text{pl}} = 0$ in eq. (4), for the sake of simplicity) is used for both phases in order to define the corresponding yield function:

$$g_\psi\left(\underset{\sim}{\boldsymbol{s}}_\psi\right) = J_2\left(\underset{\sim}{\boldsymbol{s}}_\psi\right) - R_\psi^0 \tag{13}$$

where $\psi = \alpha, \beta$, and $\underset{\sim}{\boldsymbol{s}}_{\psi}$ and R^0_{ψ} are respectively the deviatoric stress tensor and the initial yield stress in phase ψ.

A Von-Mises criterion is adopted for both phases, where $J_2 = \sqrt{\frac{3}{2}\underset{\sim}{\boldsymbol{s}}_{\psi} : \underset{\sim}{\boldsymbol{s}}_{\psi}}$.

The Normality rule for plastic flow is adopted:

$$\dot{\underset{\sim}{\boldsymbol{\varepsilon}}}^p_{\psi} = \dot{\lambda}_{\psi} \underset{\sim}{\boldsymbol{n}}_{\psi}, \quad \text{with} \quad \underset{\sim}{\boldsymbol{n}}_{\psi} = \frac{\partial g_{\psi}}{\partial \sigma_{\psi}} \tag{14}$$

As a result, two distinct plastic multipliers $\dot{\lambda}_{\alpha}$ and $\dot{\lambda}_{\beta}$ are required in the theory. They are determined independently for each phase using the consistency condition in rate–independent elasto-plasticity.

3. Parameters and conditions for FE calculations

Eqs. (1)-(3) have been recast into balances of microforces, following [1, 16], and implemented in the finite element software Z-Set [14], where balances and constitutive laws are separated. The values of the parameters entering the model are reported in non-dimensional form in Table 1, where length, time and energy scales are respectively the size L of the system (typically the average distance between precipitates), diffusion time $\tau = M/k$, and the curvature k of the free energies with respect to concentration, which is chosen to be the same for both phases ($k_{\alpha} = k_{\beta} = k$), see eq. (6). The rescaled quantities are denoted with tilde.

Table 1. Parameters in non-dimensional form.

c^e_{α}	0.7	c^e_{β}	0.3
$\widetilde{\Lambda} = \Lambda/(kL)$	5×10^{-4}	$\widetilde{\delta} = \delta/L$	5×10^{-2}
$\widetilde{D}_{\alpha} = D_{\alpha}\tau/L^2$	1×10^{-4}	$\widetilde{D}_{\beta} = D_{\beta}\tau/L^2$	1×10^{-4}
$\widetilde{E}_{\alpha} = E_{\alpha}/k$	14×10^{10}	$\widetilde{E}_{\beta} = E_{\beta}/k$	7×10^{10}
$\nu_{\alpha} = \nu_{\beta}$	0.3	$\widetilde{R}^0_{\beta} = R^0_{\beta}/k$	50
$\underset{\sim}{\boldsymbol{\varepsilon}}^{\star}$	$3 \times 10^{-4}\underset{\sim}{\mathbf{1}}$		

Although most of the values have been selected in order to comply at least qualitatively with metallic alloys and in particular with Ti alloys, different quantities have been selected so as to enhance the effects of the coupling between the $\alpha \rightarrow \beta$ transformation and plasticity with moderate strains in the validity range of the small strain framework.

In order to enhance the variations of concentrations (commensurate with $c^e_{\alpha} - c^e_{\beta}$) associated with curvature and strain/stress changes, the equilibrium concentrations are set arbitrarily to the values in the middle of range [0; 1]. Moreover, both phases are considered as elastically isotropic for simplicity, with α twice stiffer than β, i.e. $E_{\alpha} = 2\,E_{\beta}$. This ratio is likely to be greater than the real one [15], although there is a large scatter of the elastic moduli reported in the literature. But this significant contrast has been chosen to promote the heterogeneity of strain and stress fields in the dual phase microstructure even for moderate imposed strains. Finally, it can be noticed that a very small and isotropic eigenstrain $\underset{\sim}{\boldsymbol{\varepsilon}}^{\star}$ has been assigned to α so as to mimic α nodules in Ti alloys [26] which generally do not feature any orientation relationships with the β matrix.

We have considered a $L \times L$ square domain composed of a single α circular precipitate of initial radius $R^0/L = \zeta$ with $\zeta = 0.8$, surrounded by the β matrix. The system has been discretized by a

regular grid with 161 × 161 linear elements. The initial concentration in the precipitate has been set at the equilibrium concentration ($c_\alpha^0 = c_\alpha^e$), whereas β is undersaturated with $c_\beta^0 = 0.2 < c_\beta^e$ (non-dimensional initial supersaturation $\Omega^0 = (c_\beta^0 - c_\beta^e)/\Delta c^e = 0.25$, with $\Delta c^e = c_\alpha^e - c_\beta^e = 0.4$). This situation corresponds to an instantaneous heating from some temperature in the $\alpha+\beta$ field where the initial precipitate is at equilibrium up to some higher temperature still in the two-phase domain.

At the boundaries, zero fluxes are imposed for ϕ and c, i.e. $\nabla c \cdot \underline{\mathbf{n}}^{\text{ext}} = 0$ and $\nabla\phi \cdot \underline{\mathbf{n}}^{\text{ext}} = 0$ where $\underline{\mathbf{n}}^{\text{ext}}$ are the normals to the system boundaries pointing outward. Moreover, the mechanical load is applied by keeping the boundaries planar.

The loading sequences are as follows: (i) during $\Delta\widetilde{t}_1 = 1 \times 10^{-2}$, there is no load applied. (ii) Then the imposed average shear strain $\langle\epsilon_{12}\rangle$ is increased linearly during $\Delta\widetilde{t}_2 = 1 \times 10^{-1}$, up to some prescribed homogeneous shear E_{12}. (iii) This shear is sustained for a duration sufficient for the system to achieve an equilibrium state (under load). The loading sequences are shown in the inset of Fig. 1 with stage (ii) differentiated with the grey vertical slab.

4. Results

Three finite element simulations have been performed. First, a reference calculation discarding mechanics was performed. Then, two other calculations have been performed by mechanical loading for $\Delta\widetilde{t}_2 = 1 \times 10^{-1}$ up to $E_{12} = 1 \times 10^{-2}$ (shear rate $\langle\dot{\widetilde{\epsilon}}_{12}\rangle = 1 \times 10^{-1}$), considering an elastic behavior for both matrix and precipitate phases for the first case and an ideal isotropic plasticity in β matrix for the second.

The time evolution of the precipitate fraction and the concentration field of the α precipitate during the dissolution of the α precipitate are respectively shown in Fig. 1 and Fig. 2 for different cases.

As expected, for pure chemical calculations the precipitate remains circular during the whole dissolution with a decrease of the radius following a $\sqrt{t}$ law at the beginning of the process. Then, dissolution stops when the equilibrium phase fraction is reached. This equilibrium given by the lever rule $f_e = \Omega + \pi\zeta^2(1-\Omega)$ where $\Omega = (c_\beta^0 - c_\beta^e(\widetilde{R}))/\Delta c^e$ is the undersaturation accounting for the Gibbs–Thomson effect that changes the equilibrium concentrations at curved interfaces as follows $c_\psi^e(\widetilde{R}) = c_\psi^e + \widetilde{\Lambda}/(\widetilde{R}\Delta c^e)$. Hence, considering the average concentration and the final radius, the precipitate volume fraction at equilibrium is $f_\alpha = 0.38$ (upper horizontal dashed line in Fig. 1).

For the calculation where both phases are elastic, the precipitate dissolves totally during the loading stage (ii), as shown in Figs. 1 and 2a-d (middle column). The precipitate displays rapidly a nut shape with symmetry axes corresponding to the diagonals of the square system, with the long (resp. short) axis along the upper (resp. lower) diagonal. Indeed, as shown in Fig. 3, the aspect ratio l/L (short over long) of the precipitate decreases when the imposed shear strain increases linearly during the loading step. When the load is sustained, the precipitate size is sufficiently small so that the minimization of the interface energy drives the dissolution process: the aspect ratio tends to increase sharply until complete disappearance of the precipitate.

Contrary to the elastic case, the precipitate in a matrix with plastic relaxation does not dissolve totally and reaches stable size and shape on a time scale similar to the chemical case. As shown in Fig. 1, the dissolution rate is the same as in the elastic case at the beginning of the loading. Then, a deviation between both cases is observed at the middle of stage (ii). This difference in the evolutions is also clearly visible in Fig. 2 when comparing snapshots of the microstructure at same times. Starting from the same initial precipitate (top row), the shapes are already different (second row) at the middle of the loading stage (ii), i.e. at the onset of the deviation between the phase fraction curves ($\widetilde{t} = 0.04$): whereas the precipitate becomes elliptical in the elastic case, it displays a lemon shape with flat sides connected by curved segments along the diagonals. It can

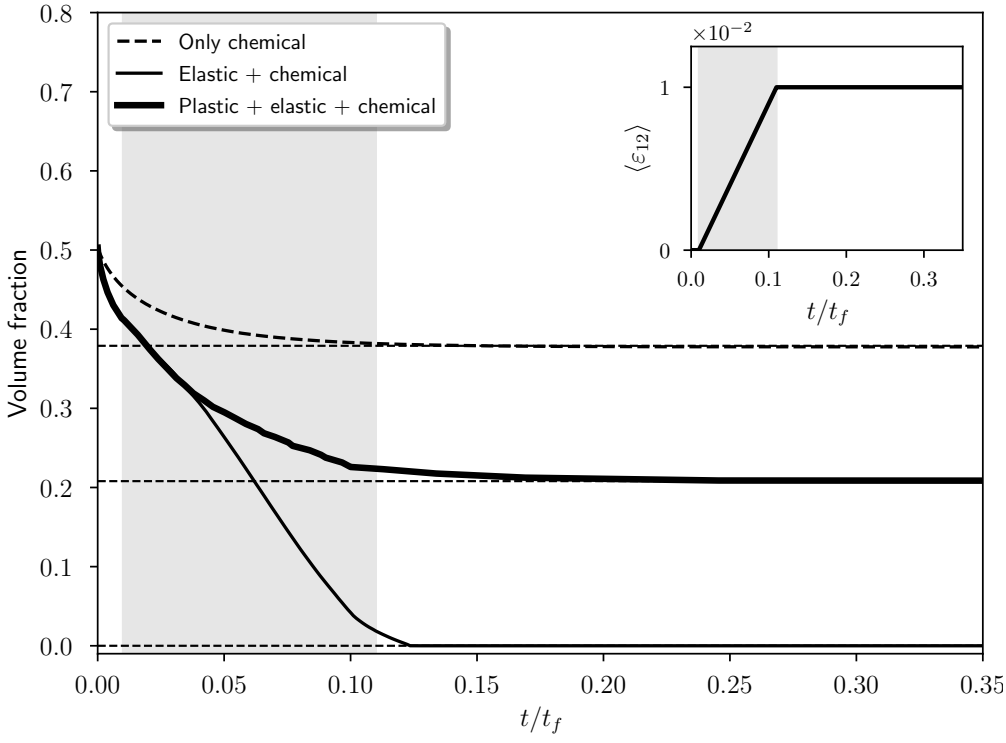

Figure 1. Precipitate fraction vs time for chemical (dashed line), elastic (thin continuous line) and plastic (thick continuous line) cases. Inset shows the average shear strain loading sequence.

also be noticed that the concentration fields in α and β phases are more heterogeneous when plastic relaxation is accounted for in β. At the end of the loading stage (ii), the shapes in both cases display sharper tips along the upper diagonal (third row), with a thinner and shorter precipitate in the elastic case, in agreement with the phase fraction (Fig. 1). In both cases, the precipitates are homogeneous in concentration when the β matrices are still heterogeneous. Finally, at the end of stage (iii), when the precipitate has already disappeared in the elastic case, the precipitate has kept the shape achieved at the end of stage (ii) with a smaller size in the plastic case. It is worth stressing that the concentration fields are homogeneous in both phases, indicating that chemical equilibrium has been achieved. Moreover, in the plastic case, the aspect ratio l/L in Fig. 3 decreases almost linearly with time during the loading stage (ii), before stopping around 0.58 with a very slow evolution towards the equilibrium value ≈ 0.55.

For the plastic case, we have plotted in Fig. 4 snapshots of the cumulative plastic strain p as well as the hydrostatic pressure taken here as one third of the trace of the stress tensor at different times. Plastic relaxation starts in the first part of the loading stage (ii), with bands forming approximately parallel to the system boundaries, in agreement with previous works in nonlinear composites [7, 23]. They are more intense close to the precipitate tips along the upper diagonal due to the asymmetrical shape of the precipitate (Fig. 4b). At the end of the loading stage, the bands are thicker due to the dissolution of the precipitate, with "hot spots" where $p \approx 2\%$ along the upper diagonals. At the end of stage (iii), the four bands enclosing the precipitate are thick with large "hot spots" ($p \approx 3\%$) along the upper diagonal. During the last stage where the evolution of the precipitate is minor, small "hot spots" appear also along the

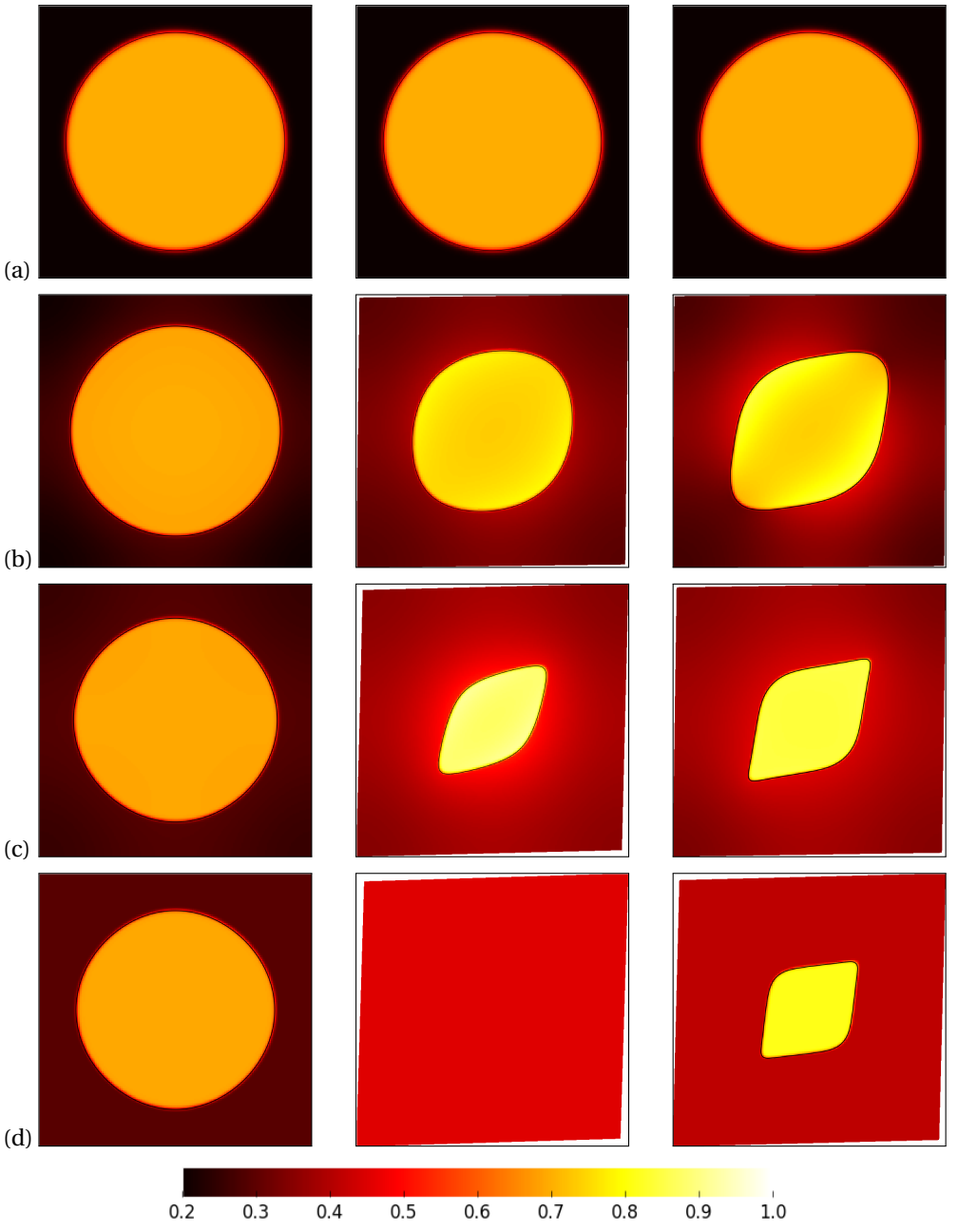

Figure 2. Snapshots of the concentration field during the dissolution of the α precipitate in the chemical (first column), elastic (middle column) and plastic (last column) cases at (a) $\widetilde{t} = 10^{-3}$, (b) $\widetilde{t} = 4 \times 10^{-2}$, (c) $\widetilde{t} = 10^{-1}$, and (d) $\widetilde{t} = 1$; with $\widetilde{t} = t/t_f$.

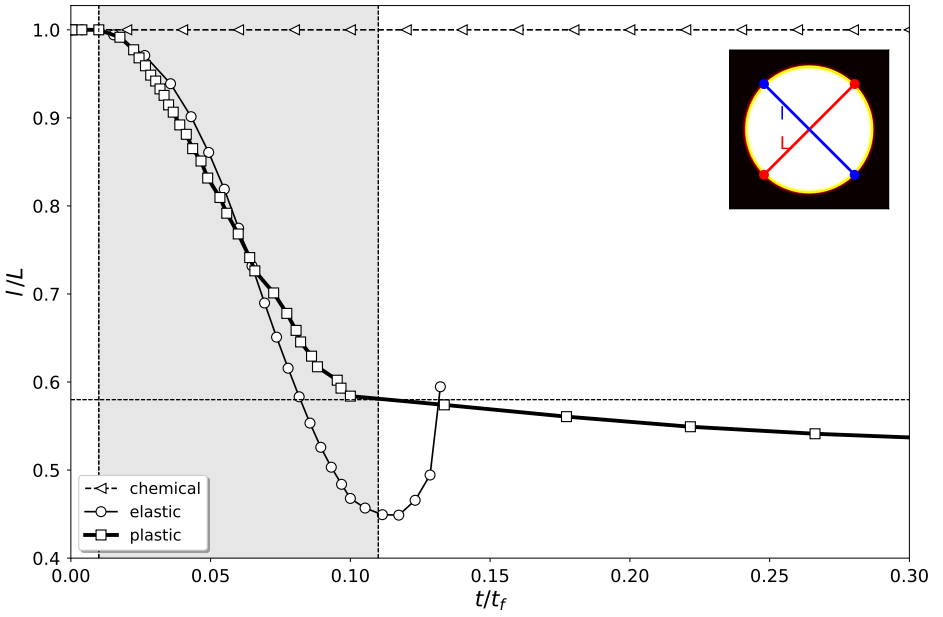

Figure 3. Aspect ratio of the precipitate l/L vs. time for the chemical, elastic and plastic cases.

lower diagonal. It is clear that the patterning of plasticity is tightly coupled to the microstructure evolution. The pressure distribution is characterised by significant but realistic values with maximal values concentrated at regions close to highly curved precipitate boundaries. These locations are correlated with intense strain localization zones.

The shape evolutions can be understood by analyzing the evolution of the concentration fields. Indeed, the local interface velocity is related to the difference of flows between α and β phases as stated by the interface solute balance:

$$\Delta c\, v = D\left(\nabla c_\beta - \nabla c_\alpha\right)\cdot \underline{\mathbf{n}} \tag{15}$$

with all quantities considered at the α/β interface, $\Delta c = c_\alpha - c_\beta$ where $\underline{\mathbf{n}}$ denotes the normal vector pointing from α to β.

Hence, we have plotted the concentration profiles at different time steps in Fig. 5 (c to e corresponding to the loading stage (ii)), along the left and right diagonals of the system drawn respectively with red and blue lines in the upper left snapshot. The elastic and plastic cases are plotted with dashed and continuous lines respectively.

It can be noted that the concentration field becomes rapidly heterogeneous in α and β. At the beginning of the shear loading ($\widetilde{t} = 3.0 \times 10^{-2}$, Fig . 5a), the concentrations are higher than in the bulks, such that diffusion in α and β phases promotes the dissolution according to the interfacial solute balance eq. (15) ($\nabla c_\alpha \cdot \underline{\mathbf{n}} > 0$ and $\nabla c_\beta \cdot \underline{\mathbf{n}} < 0$). The circular symmetry is slightly broken as illustrated by the differences between the left and right profiles corresponding to the two diagonals. The gradients are steeper along the lower diagonal (right) in agreement with the shape evolutions ensuing from a faster dissolution along this diagonal. Moreover, the plastic case is more asymmetrical than the elastic case, with slightly higher interfacial concentrations. It can also be noticed that the interface concentrations are higher than the equilibrium concentrations at flat interfaces (horizontal dashed lines at 0.3 and 0.7 for respectively β and α). Finally, due to

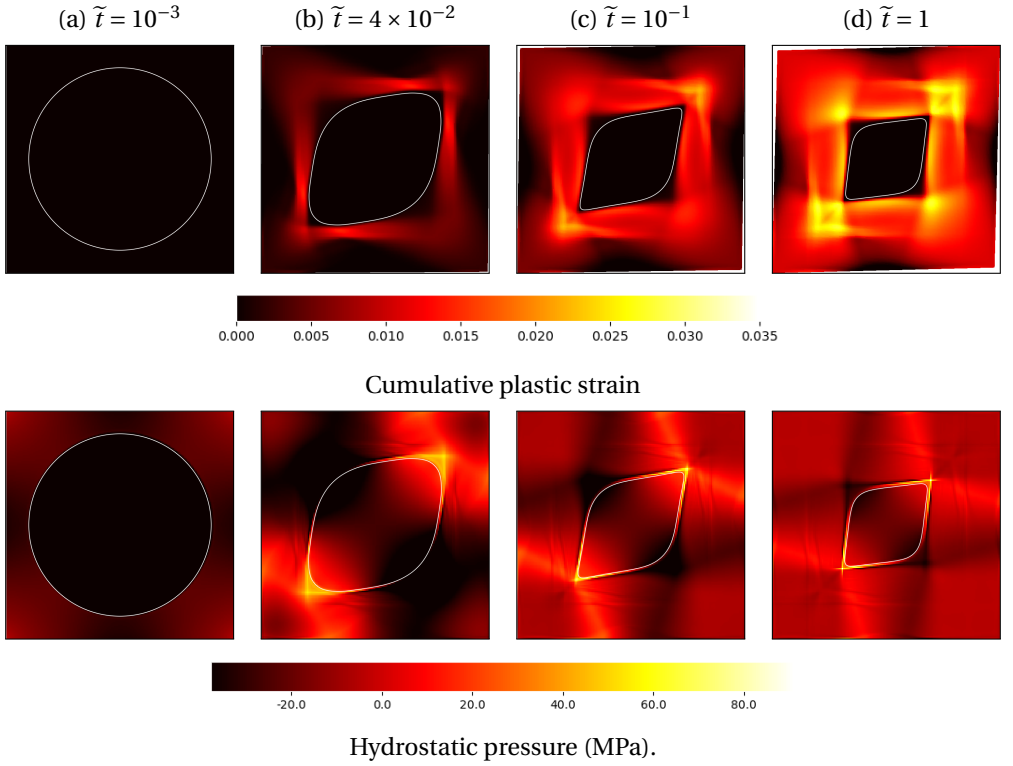

Figure 4. Snapshots of cumulative plastic strain and hydrostatic pressure during shear loading at rate $\langle \dot{\widetilde{\varepsilon}}_{12} \rangle = 0.1$

the initial undersaturation of the β matrix, the concentration gradients are steeper in β and are likely to drive the dissolution process at this stage.

During stage (ii), elastic and plastic cases exhibit different evolutions of the concentration profiles. First, at the middle of the loading stage $\widetilde{t} = 7.5 \times 10^{-2}$ (Fig. 5b), when the size of the precipitates are still similar, the asymmetry becomes much stronger in the plastic case. Whereas concentration gradients are still in a configuration promoting dissolution in the elastic case, the plastic case features two different behaviors depending on the diagonal. Hence, along the upper diagonal, one can observe the inversion of ∇c_α (i.e. $\nabla c_\alpha \cdot \underline{\mathbf{n}} < 0$) and the drastic lowering of $|\nabla c_\beta|$. Quantitatively, $(\nabla c_\beta - \nabla c_\alpha) \cdot \underline{\mathbf{n}} \approx 0$ such that the interface along the upper diagonal does not migrate any longer. On the contrary, the profiles along the lower diagonal remain favorable to the dissolution with $\nabla c_\alpha \cdot \underline{\mathbf{n}} > 0$ and $\nabla c_\beta \cdot \underline{\mathbf{n}} < 0$. As the shear load increases (Fig. 5c-e), in the elastic case, the concentration in the α precipitate increases continuously as well as the interface concentration in β. Consequently, the gradients increase such that the dissolution rate increases with time to end up with the total disappearance of the precipitate at the end of stage (ii). In the plastic case, the asymmetry between the profiles along the diagonal decreases during stage (ii). When the profile evolves only slowly and slightly along the upper diagonal, so that the interface migration is negligible, the profiles become flatter along the lower diagonal with an enrichment of the β matrix, so that dissolution along this diagonal slows down progressively. At the end of stage (iii), the profiles in the plastic case are flat in the bulks with concentrations higher than the equilibrium concentrations for flat interfaces (Fig. 5e).

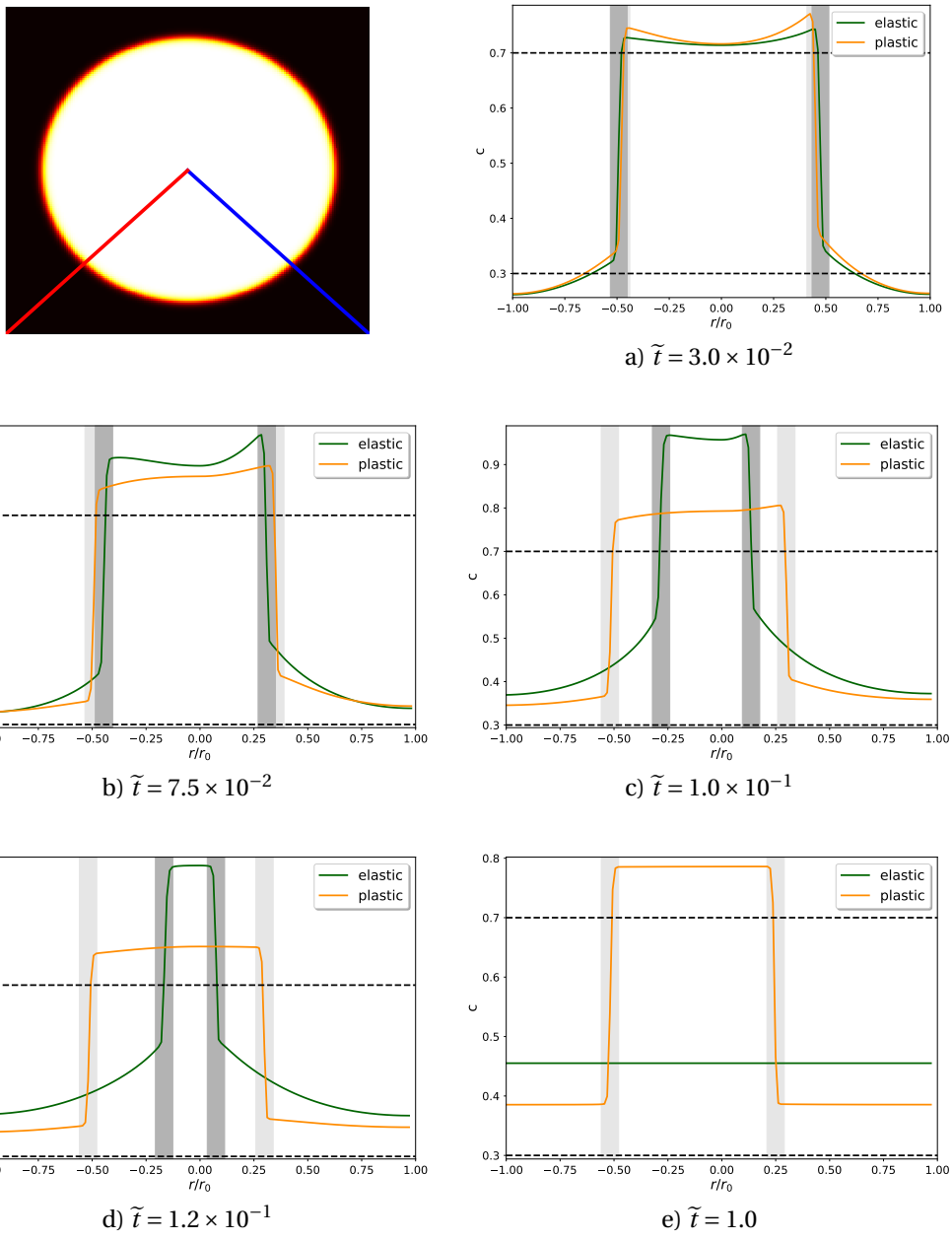

Figure 5. Concentration profiles along the left and right diagonals at different time steps in the elastic (dashed line) and plastic (continuous line) cases. The plot axis is drawn in the upper left snapshot by the red and blue lines, respectively for left and right half-diagonals. Equilibrium concentrations $c_\alpha^e = 0.7$ and $c_\beta^e = 0.3$ of flat interfaces are plotted with dashed horizontal lines.

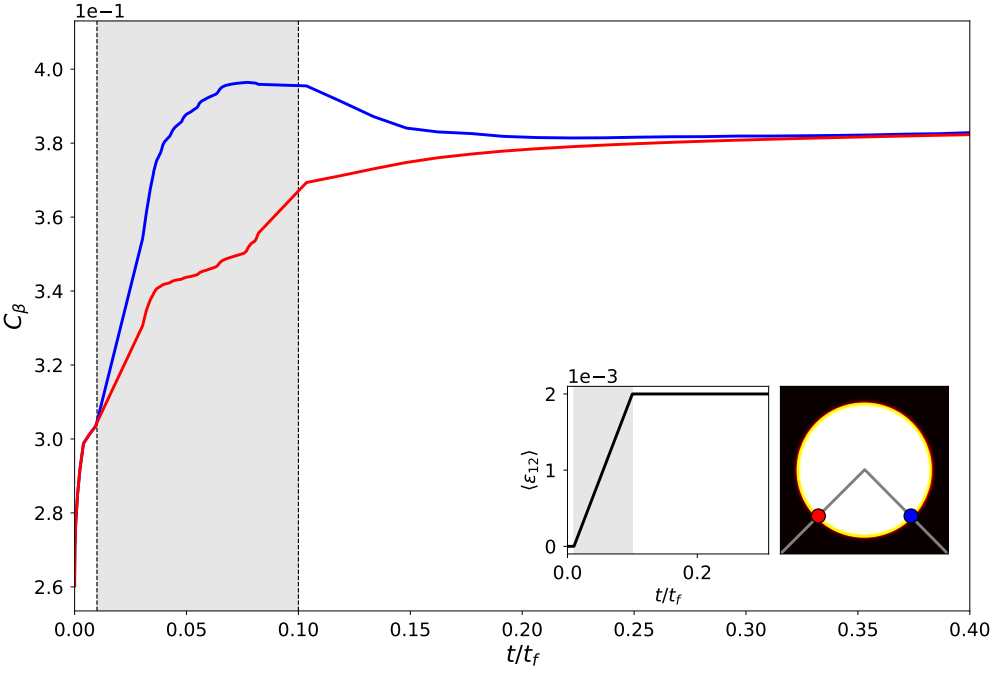

Figure 6. Time evolution of the concentrations in β at the interfaces crossing respectively the left (red) and right (blue) half-diagonals, in the plastic case.

The previous analysis suggests that the interfacial concentrations are a key parameter controlling the shape evolutions through the concentration fields. Indeed, we have mentioned that the amplitude and sign of the solute flows are driven by the evolution of these concentrations. Thus, we have determined the interfacial concentrations by extrapolating the bulk profiles (typically close to $\phi = 0.05$ or 0.95) into the diffuse interface and extracting the values at $\varphi = 0.5$.

We have plotted in Fig. 6 the concentration in β at the interfaces crossing the upper (red) and lower (blue) diagonals respectively, in the plastic case. It must be stressed that the small irregularities observed in the curves should be attributed to some numerical problems but rather to the sensitivity of the extraction method to the order and support of the extrapolation from the bulks. After a transient regime, shorter than $\widetilde{t} = 10^{-2}$ during the load free stage (i), the interface concentration reaches its equilibrium value accounting for the Gibbs–Thomson effect, i.e. with a value slightly above 0.3 increasing with the local curvature. When the shear load is applied, the concentrations at the two different interfaces increase with different rates that do not involve only the change in local curvatures. Indeed, whereas the interface crossing the lower diagonal is flatter than the interface crossing the upper diagonal (Fig. 2b last column), its concentration increases the fastest. When the concentration of the sharper tips (red) with the slow migration rate increases continously, with a sudden deceleration around $\widetilde{t} \approx 0.04$, the evolution of the concentration on the flatter sides (blue) displays a maximum by the end of stage (ii). Then, during stage (iii) the concentrations at both interfaces converge slowly towards the same value of about 0.38.

To understand these evolutions, we have proceeded as in [4, 10] by comparing the interfacial concentrations with their expressions at a sharp interface in local equilibrium, accounting for mechanics. Following [29], these concentrations can be obtained using the equilibrium

conditions holding at a coherent sharp interface:

$$\Delta\mu = 0 \tag{16}$$

$$\Delta\omega = E_{\text{coh}} - \Lambda\kappa \tag{17}$$

where Δ denotes as previously the difference between the α and β sides of the interface (i.e. $\Delta A = A^{\alpha} - A^{\beta}$ for any A), $\mu = \partial f/\partial c$ the diffusion potential, $\omega = f - \mu c$ the grand potential, κ the local curvature (positive for convex α), and $E_{\text{coh}} = \sigma_{\beta} : \Delta\varepsilon$ the coherence energy, representing the elastic energy necessary to keep both lattices coherent across the interface [20,21]. It is worth noting that eqs. (16)-(17) reduce to the usual equality of the chemical potentials between both phases when elasticity and curvature can be neglected.

As introduced in the phase field model Section 2, the free energy densities f can be split into chemical and elastic contributions. Because it is assumed that the elastic energy does not depend on c, the diffusion potentials are independent of stress and the grand potential can be rewritten as $\omega = f_{\text{ch}} + f_{\text{el}} - \mu c$. Then, expanding eqs. (16)-(17) to first order in c with respect to the chemical equilibrium holding at flat interfaces (where the right-hand side of eq. (17) is null), one obtains:

$$\Delta\left(\frac{\partial\mu_{\text{ch}}}{\partial c}\left(c - c^{e}\right)\right) = 0 \tag{18}$$

$$\Delta\left(-c^{e}\frac{\partial\mu_{\text{ch}}}{\partial c}\left(c - c^{e}\right) + f_{\text{el}}\right) = E_{\text{coh}} - \Lambda\kappa \tag{19}$$

Using the fact that the curvatures of f with respect to c (i.e. $\partial\mu_{\text{ch}}/\partial c$) are the same for α and β, eqs. (18)-(19) become:

$$\begin{aligned} c_{\alpha}^{e} - c_{\beta}^{e} &= \Delta c^{e} \\ c_{\psi} - c_{\psi}^{e} &= \frac{\widetilde{\mathscr{E}} + \widetilde{\Lambda}\widetilde{\kappa}}{\Delta c^{e}} \qquad \forall\ \psi \in \{\alpha, \beta\} \end{aligned} \tag{20}$$

where the non-dimensional mechanical contribution to the change in the interfacial concentrations reads:

$$\widetilde{\mathscr{E}} = \frac{\Delta f_{\text{el}} - E_{\text{coh}}}{k} \tag{21}$$

We have shown in [3] that this expression still holds when plastic strain is accounted for, and that plastic strain directly contributes to the change in the local equilibrium through the jump of strain $\Delta\underset{\sim}{\boldsymbol{\varepsilon}}$ across the interface. It must be emphasized that the presence of the coherency term discard any simple explanations based only on the distribution of the elastic energy density.

Following the same procedure as for the interfacial concentrations, we have extrapolated all the quantities involved in eq. (21) in the bulks near the interface up to $\phi = 0.5$, namely Δf_{el} and E_{coh} to determine the evolution of the mechanical contribution $\widetilde{\mathscr{E}}$. In this way, we have checked that the evolution of the interfacial concentrations (Fig. 6) can be explained by the modification of the local equilibrium by elasto-visco-plasticity. Although the extraction method of the interfacial quantities is not robust enough to verify precisely eq. (20), we have checked that the order of magnitude of the variations are consistent with this expression. Fig. 7 shows the evolution with respect to time of the two contributions $\Delta f_{\text{el}}/k$ and E_{coh}/k in insets as well as the resulting $\widetilde{\mathscr{E}}$. First, it can be noticed that the variations of the coherence energy are larger than the variations of the jump in elastic energy. Moreover, the coherence energy is almost always negative, thus contributing positively to the mechanical term $\widetilde{\mathscr{E}}$ (eq. (21)). Second, two very different behaviors are observed at the two kinds of interfaces, crossing the upper (red) and lower (blue) diagonals, corresponding respectively to the tips and to the rounded sides (Fig. 2 last column). At the "red" interface, both Δf_{el} and E_{coh} evolve in the same direction during the loading stage (ii), with a first increase from negative values to positive ones, followed by large drops to negative values. Consequently, the evolution of $\widetilde{\mathscr{E}}$ displays two steps during stage (ii): a first drop to around zero when plastic "hot spots" are not visible yet ahead of the tips (Fig. 4b), followed by a large increase

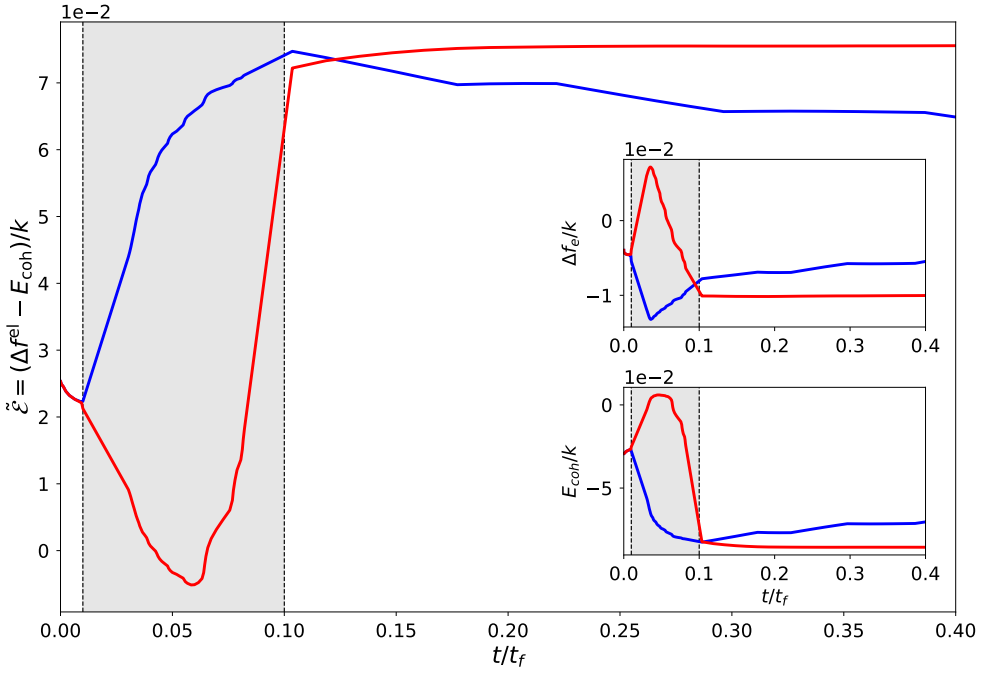

Figure 7. Time evolution of the mechanical energy contribution to the interfacial local equilibrium at interfaces crossing respectively the left (blue) and right (red) diagonals (see inset in Fig. 6), in the plastic case.

when the "hot spots" intensify (Fig. 4c). Hence, these two steps can explain the evolution of the interfacial concentration. When $\widetilde{t} \lessapprox 0.04$, the increase of c_β can be attributed to the combined effect of $\widetilde{\mathscr{E}}$ and curvature with the appearance of the nut shape with tips along the upper diagonal (Fig. 4b). Then the sudden slowdown is likely due to $\widetilde{\mathscr{E}} < 0$ that cancels the curvature term although the tips sharpen significantly (Fig. 4c). Finally, when $\widetilde{\mathscr{E}}$ has increased again sufficiently, it takes over and the increase of c_β accelerates again. During stage (iii), all contributions evolve only slightly and slowly. It can be observed that the tips do not sharpen any longer and the slight increase of the interface concentrations can be attributed to the slight plastic relaxation at constant shear load. At the "blue" interface, the coherence energy E_{coh} remains negative and always overcomes the jump in elastic energy density Δf_{el}. This is why the evolution of $\widetilde{\mathscr{E}}$ follows mainly that of $-E_{\mathrm{coh}}$, with a steep increase in the first half of stage (ii), followed by a progressive slowdown. Finally, during stage (iii) all evolutions are slow and moderate resulting in a slight decrease of $\widetilde{\mathscr{E}}$. As for the "red" interface, the overall evolution of $\widetilde{\mathscr{E}}$ can explain the evolution of c_β: a steep increase at the beginning of stage (ii), followed by a slight decrease during stage (iii), although the max of c_β is achieved before the end of stage (ii) whereas $\widetilde{\mathscr{E}}$ is maximal at the transition between stages (ii) and (iii).

In conclusion, this analysis has shown that the two different dissolution rates along the upper and lower diagonals result from the particular pattern of plastic strain: the plastic case is not a tempered elastic case, but plastic relaxation plays a significant role in the morphological evolution of the precipitates in the particular situation investigated.

Finally, the previous calculations may give clues about what can happen in adiabatic shear bands in Ti forged parts where globular precipitates are observed to be much smaller than in other parts. Indeed, they are usually attributed to either the complete dissolution followed

by nucleation of new small precipitates on defects, or the splitting of surviving precipitates. Nonetheless, the splitting process is never explained and it is not clear how dissolution and mechanics interact.

Using the previous calculation accounting for plasticity as a reference, we have considered higher loading rates and a higher sustained shear (thereafter, referred to as cases 1 and 2 respectively):

- $\langle \dot{\widetilde{\varepsilon}}_{12} \rangle = 1$ during $\Delta \widetilde{t}_2 = 10^{-2}$ up to $E_{12} = 10^{-2}$;
- $\langle \dot{\widetilde{\varepsilon}}_{12} \rangle = 10$ during $\Delta \widetilde{t}_2 = 10^{-3}$ up to $E_{12} = 10^{-2}$.

Indeed, we can expect that increasing the shear magnitude will enhance dissolution, and that increasing the shear rates, the time scale of mechanics will compete with the time scale of diffusion.

In Fig. 8, we have plotted snapshots of concentration and accumulated plastic strain during the dissolution, for the first rate $\langle \dot{\widetilde{\varepsilon}}_{12} \rangle = 1$. Because the loading rate is larger than in the reference case, the second snapshot at $\widetilde{t} = 0.015$ is already in stage (iii). This second snapshot exhibits the same shape evolution as in the reference case, the precipitate adopting a lemon shape with tips along the upper diagonal. The overall pattern of cumulative plastic strain is similar to the reference case, with two sets of bands aligned with the system boundaries and more intense close to the tips. Due to the higher sustained shear load, p reaches higher values with respect to Fig. 4. Contrary to the reference case, p extends also off the horizontal and vertical bands, along the two diagonals in the matrix. At the same time, the heterogeneity in concentration is more pronounced with rich regions close to the interfaces oriented in the same direction as the upper diagonal. Nonetheless, comparing Fig. 8b and Fig. 2b (last column), the difference seems only to be quantitative rather than qualitative. This is why, the elongated shape at $\widetilde{t} = 0.1$ can appear as unexpected. In fact, this shape results from the same differentiated dissolution as in the reference case, i.e. fast dissolution along the lower diagonal and pinning of the interfaces along the upper diagonal by the particular configuration of solute profiles. Plastic patterning remains qualitatively similar to earlier times, with bands slightly thicker and more intense. Then, the dissolution continues along the lower diagonal only so that the precipitate pinches off (Fig. 8c) to finally split into two precipitates (Fig. 8d). It is worth noticing that the pattern of cumulative plastic strain remains almost the same during this process ($\widetilde{t} \geq 0.1$): the size of the square with no plastic strain is related to the most distant interfaces along the upper diagonal. Nonetheless, very thin plastic bands can be observed at the center of the system.

The evolution of the microstructure during the second intense shear loading with the fastest rate $\langle \dot{\widetilde{\varepsilon}}_{12} \rangle = 10$ is plotted in Fig. 9. In this case, the shape at $\widetilde{t} = 0.015$ is different from the previous cases. Smooth corners, visible at about 30° from the upper diagonal, separate the interface into two parts: segments with normal vectors closer to the lower diagonal with large solute gradients; segments with normal vectors closer to the upper diagonal with vanishing solute gradients. The corresponding cumulative plastic strain displays a pattern similar to case 1, with more intense values and additional bands at 45°. As shown in Fig. 8c, contrary to case 1, dissolution is not the fastest along the lower diagonal but next to the smooth corners. This process results in splitting the initial precipitate into three parts. The precipitate at the center features a shape reminiscent of the reference case. It displays a very high concentration and is surrounded by an enriched zone coming from the fast dissolution process, that will drive its complete dissolution. The two other precipitates display asymmetrical shapes with the longest axis along the lower diagonal. The configuration of the solute field in the matrix with almost no gradient oriented normal to their interfaces explains why they will survive (Fig. 8 d). The complete dissolution of the central precipitate is fast so that only thin and slight plastic bands enclosing it have time to develop.

To understand why increasing the shear load and the shear rate promotes the splitting of

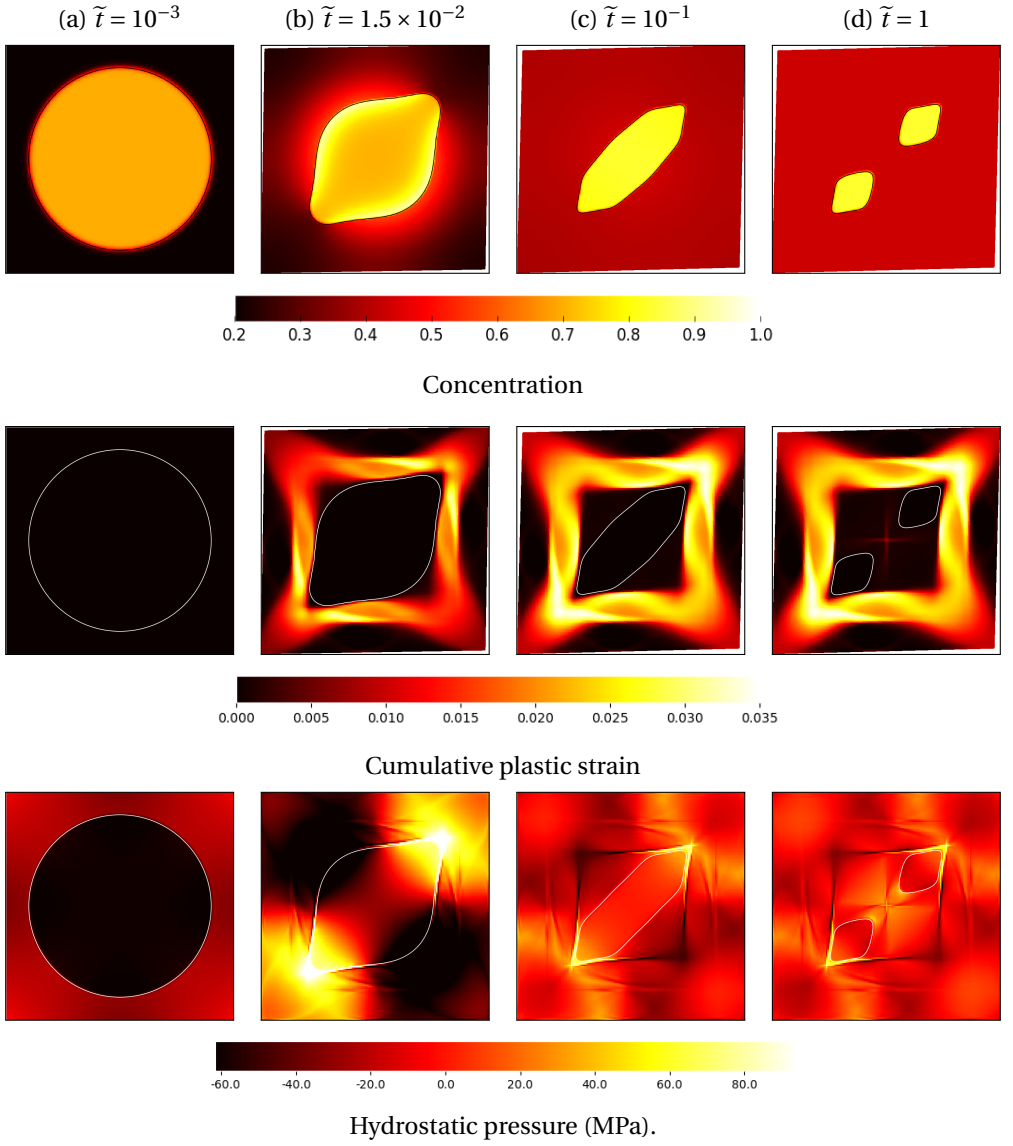

Figure 8. Snapshots of concentration, cumulative plastic strain and hydrostatic pressure during intense shear loading at rate $\langle \dot{\widetilde{\varepsilon}}_{12} \rangle = 1$.

precipitates, it is important to have in mind the analysis based on the solute balance eq. (15) and the local equilibrium condition eqs. (20)-(21).

- First, increasing the shear load increases locally the concentration at the interfaces making significant angles with the lower diagonal, but does not change the situation at the interfaces crossing the upper diagonal. Indeed, the pattern of plastic relaxation remains qualitatively the same with a major localization along the upper diagonal, responsible for the pinning of the neighboring interfaces. Thus, the differential dissolution is not changed with respect to the reference case.
- Second, increasing sufficiently the shear rate implies that diffusion becomes too slow to

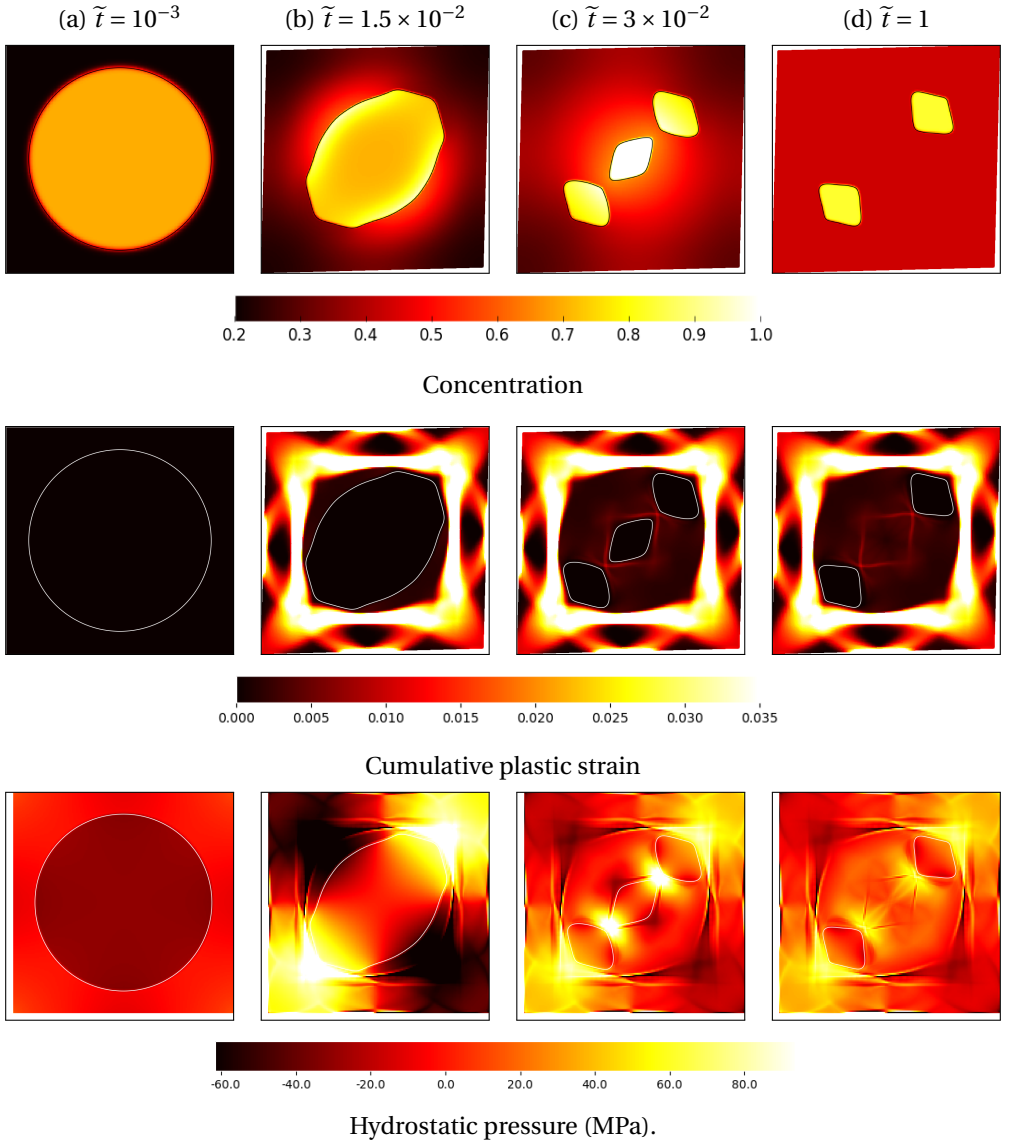

Figure 9. Snapshots of concentration, cumulative plastic strain and hydrostatic pressure during intense shear loading at rate $\langle \dot{\widetilde{\varepsilon}}_{12} \rangle = 10$.

mitigate the concentration gradients enhanced by the change in the interfacial concentrations. Hence, contrary to the reference case, dissolution in the direction of the lower diagonal can proceed to completion and splits the precipitate.

With these calculations, we have shown that the production of small precipitates from large ones is possible by plasticity-assisted dissolution provided that the ratio of the loading time scale over the diffusion time scale is lowered. The precise value of the critical ratio beyond which splitting is possible has not been determined because it is very dependent on the configuration considered. Further work is obviously needed to obtain more quantitative information, in particular by considering 3D, different spatial distributions and more complex loadings. Moreover, it

is likely that work-hardening, plasticity within the precipitates, and anisotropy associated with crystal plasticity, which were not considered in the present work, will definitely play a role. These considerations also bring the question of inheritance of plastic activity and dislocation hardening. Indeed, in the case of growth some aspects of this question have been addressed in [4] and have been shown to change the morphological evolutions.

5. Conclusion

We have investigated the influence of plasticity on the dissolution of precipitates at high temperatures in the case of shear loading. We have shown that plasticity is able to stabilize precipitates that dissolve completely when only elasticity is accounted for. Moreover, we have deeply investigated the process giving rise to the nut shapes, whose symmetry reflects those of the precipitate arrangement and loading. In particular, we have demonstrated that plasticity modifies the local equilibrium at the interface and consequently the local dissolution rate. In the investigated configuration, strong localization of plastic strain in the matrix tends to pin the neighboring interface so that the initial circular symmetry is broken. It remains to analyse more in detail the relative contributions of various terms in the driving force responsible for precipitate evolution. They include the impact of heterogeneous elasticity, of phase transformation eigenstrain and of plastic eigenstrain tensors. Preliminary calculations have shown that different non isotropic shapes can be obtained depending on these different contributions to the driving force.

Finally, we have studied intense and rapid shear loadings. When diffusion is not sufficiently fast to homogenize the concentration field generated by the change in interfacial concentrations associated with mechanics, dissolution that proceeds at different rates along the interface leads to the splitting of the initial precipitate into several ones. Hence, our work may give clues about the process explaining the presence of small precipitates in adiabatic shear bands in forged parts in titanium alloys, although further work is needed to obtain more quantitative predictions.

Acknowledgments

BA acknowledges Yann Le Bouar and Alphonse Finel for strong interactions, either short or long range.

References

[1] K. Ammar, B. Appolaire, G. Cailletaud, F. Feyel, S. Forest, “Finite element formulation of a phase field model based on the concept of generalized stresses”, *Comput. Mater. Sci.* **45** (2009), no. 3, p. 800-805.
[2] K. Ammar, B. Appolaire, G. Cailletaud, S. Forest, “Combining phase field approach and homogenization methods for modelling phase transformation in elastoplastic media”, *Eur. J. Comput. Mech.* **18** (2009), no. 5-6, p. 485-523.
[3] ———, “Phase field modeling of elasto-plastic deformation induced by diffusion controlled growth of a misfitting spherical precipitate”, *Philos. Mag. Lett.* **91** (2011), no. 3, p. 164-172.
[4] K. Ammar, B. Appolaire, S. Forest, M. Cottura, Y. Le Bouar, A. Finel, “Modelling inheritance of plastic deformation during migration of phase boundaries using a phase field method”, *Meccanica* **49** (2014), p. 2699-2717.
[5] A. Basak, V. I. Levitas, “Finite element procedure and simulations for a multiphase phase field approach to martensitic phase transformations at large strains and with interfacial stresses”, *Comput. Methods Appl. Mech. Eng.* **343** (2019), p. 368-406.
[6] J. W. Cahn, F. Larché, “A simple model for coherent equilibrium”, *Acta Metallurgica* **32** (1984), no. 11, p. 1915-1923.
[7] J.-L. Chaboche, S. Kruch, J.-F. Maire, T. Pottier, “Towards a micromechanics based inelastic and damage modeling of composites”, *Int. J. Plast.* **17** (2001), p. 411-439.
[8] T.-L. Cheng, Y.-H. Wen, J. A. Hawk, “Modeling elasto-viscoplasticity in a consistent phase field framework”, *Int. J. Plast.* **96** (2017), p. 242-263.
[9] M. Cottura, B. Appolaire, A. Finel, Y. Le Bouar, “Phase field study of acicular growth: Role of elasticity in Widmanstätten structure”, *Acta Mater.* **72** (2014), p. 200-210.

[10] ———, "Plastic relaxation during diffusion-controlled growth of Widmanstätten plates", *Scr. Mater.* **108** (2015), p. 117-121.
[11] ———, "Coupling the Phase Field Method for diffusive transformations with dislocation density-based crystal plasticity: Application to Ni-based superalloys", *J. Mech. Phys. Solids* **94** (2016), p. 473-489.
[12] ———, "Microstructure evolution under [110] creep in Ni-base superalloys", *Acta Mater.* **212** (2021), article no. 116851.
[13] M. Cottura, Y. Le Bouar, B. Appolaire, A. Finel, "Rôle of elastic inhomogeneity in the development of cuboidal microstructures in Ni-based superalloys", *Acta Mater.* **94** (2015), p. 15-25.
[14] École des Mines ParisTech (France) and Onera – the French Aerospace Lab, "Z-set package: Non-linear material & structure analysis suite", 2013, http://www.zset-software.com.
[15] E. S. Fisher, C. J. Renken, "Single-crystal elastic moduli and the hcp → bcc transformation in Ti, Zr, and Hf", *Phys. Rev.* **135** (1964), no. 2A, p. 482-494.
[16] E. Fried, M. E. Gurtin, "A phase-field theory for solidification based on a general anisotropic sharp-interface theory with interfacial energy and entropy", *Phys. D* **91** (1996), no. 1-2, p. 143-181.
[17] A. Gaubert, Y. Le Bouar, A. Finel, "Coupling phase field and viscoplasticity to study rafting in Ni-based superalloys", *Philos. Mag.* **90** (2010), no. 1-4, p. 7-28.
[18] J. Hektor, M. Ristinmaa, H. Hallberg, S. A. Hall, S. Iyengar, "Coupled diffusion-deformation multiphase field model for elastoplastic materials applied to the growth of Cu_6Sn_5", *Acta Mater.* **108** (2016), p. 98-109.
[19] C. Hermann, E. Schoof, D. Schneider, F. Schwab, A. Reiter, M. Selzer, N. Britta, "Multiphase-field model of small strain elasto-plasticity according to the mechanical jump conditions", *Comput. Mech.* **62** (2018), p. 1399-1412.
[20] W. C. Johnson, J. I. D. Alexander, "Interfacial conditions for thermomechanical equilibrium in two-phase crystals", *J. Appl. Phys.* **59** (1986), no. 8, p. 2735-2746.
[21] F. Larché, J. W. Cahn, "A linear theory of thermochemical equilibrium of solids under stress", *Acta Metallurgica* **21** (1973), no. 8, p. 1051-1063.
[22] Y. Le Bouar, A. Loiseau, A. Finel, "Origin of the complex wetting behavior in Co-Pt alloys", *Phys. Rev. B* **68** (2003), article no. 224203.
[23] H. Moulinec, P. Suquet, "Intraphase strain heterogeneity in nonlinear composites: a computational approach", *Eur. J. Mech., A, Solids* **22** (2003), p. 751-770.
[24] V. de Rancourt, K. Ammar, B. Appolaire, S. Forest, "Homogenization of viscoplastic constitutive laws within a phase field approach", *J. Mech. Phys. Solids* **88** (2016), p. 291-319.
[25] D. Schneider, S. Schmid, M. Selzer, T. Böhlke, B. Nestler, "Small strain elasto-plastic multiphase-field model", *Comput. Mech.* **55** (2014), p. 27-35.
[26] S. L. Semiatin, S. L. Knisley, P. N. Fagin, F. Zhang, D. R. Barker, "Microstructure Evolution during Alpha-Beta Heat Treatment of Ti-6Al-4V", *Metall. Mater. Trans.* **34** (2003), p. 2377-2386.
[27] M. E. Thompson, C. S. Su, P. W. Voorhees, "The equilibrium shape of a misfitting precipitate", *Acta Metallurgica and Materialia* **42** (1994), no. 6, p. 2107-2122.
[28] A. Vattré, C. Denoual, "Polymorphism of iron at high pressure: A 3D phase-field model for displacive transitions with finite elastoplastic deformations", *J. Mech. Phys. Solids* **92** (2016), p. 1-27.
[29] P. W. Voorhees, W. C. Johnson, "The Thermodynamics of Elastically Stressed Crystals" (H. Ehrenreich, F. Spaepen, eds.), Solid State Physics, vol. 59, Elsevier, 2004, p. 1-201.
[30] P. W. Voorhees, G. B. McFadden, R. F. Boisvert, D. I. Meiron, "Numerical simulation of morphological development during Ostwald ripening", *Acta Metallurgica* **36** (1988), no. 1, p. 207-222.